# High Latitude HI in NGC 2613: Buoyant Disk-Halo Outflow

Judith A. Irwin & Tara Chaves

Dept. of Physics, Queen's University, Kingston, Canada, K7L 3N6 irwin@astro.queensu.ca, tchaves@astro.queensu.ca

## ABSTRACT

We combine new VLA D array HI data of NGC 2613 with previous high resolution data to show new disk-halo features in this galaxy. The global HI distribution is modeled in detail using a technique which can disentangle the effects of inclination from scale height and can also solve for the average volume density distribution in and perpendicular to the disk. The model shows that the galaxy's inclination is on the low end of the range given by Chaves & Irwin (2001) and that the HI disk is thin ( $z_e = 188 \text{ pc}$ ), showing no evidence for halo.

Numerous discrete disk-halo features are observed, however, achieving z heights up to 28 kpc from mid-plane. One prominent feature in particular, of mass,  $8 \times 10^7 \,\mathrm{M}_{\odot}$  and height, 22 kpc, is seen on the advancing side of the galaxy at a projected galactocentric radius of 15.5 kpc. If this feature achieves such high latitudes because of events in the disk alone, then input energies of order  $\sim 10^{56}$  ergs are required. We have instead investigated the feasibility of such a large feature being produced via buoyancy (with drag) within a hot, pre-existing X-ray corona. Reasonable plume densities, temperatures, stall height ( $\sim 11 \,\mathrm{kpc}$ ), outflow velocities and ages can indeed be achieved in this way. The advantage of this scenario is that the input energy need only be sufficient to produce blow-out, a condition which requires a reduction of three orders of magnitude in energy. If this is correct, there should be an observable X-ray halo around NGC 2613.

Subject headings: galaxies: individual (NGC 2613), ISM: bubbles, galaxies: halos

## 1. Introduction

High latitude HI in disk galaxies is increasingly being recognized as an important tracer of disk activity and dynamics. The gas scale height is a measure of time integrated activity

in the disk and discrete features trace the level of local activity. The disk-halo interface represents a severe transition between two very different environments: the high density, low velocity dispersion disk and the low density, high velocity dispersion halo. Globally, it may provide information on the shape of the dark matter halo (e.g. Olling & Merrifield 2000). In a few recent cases, lagging HI halos have also been detected, such that the high latitude gas is rotating  $\sim 20$  - 50 km s<sup>-1</sup> more slowly than the underlying disk (Schaap, Sancisi, & Swaters 2000, Fraternali et al. 2001, Lee et al. 2001, Rand 2000 and Tüllmann et al. 2000). Explanations for such lags have focussed mainly on galactic fountains (cf. Bregman 1980, Swaters et al. 1997, Schaap et al. 2000, Collins et al. 2002). Edge-on galaxies are particularly useful in the study of the disk-halo region and, in this paper, we especially wish to investigate how discrete disk-halo features can be used as probes of the environment into which they are emerging.

The edge-on galaxy, NGC2613 (D = 25.9 Mpc) is a good candidate for such a study. In Paper I (Chaves & Irwin 2001), we presented Very Large Array (VLA) C Array observations of this galaxy. The resulting C array zeroth moment map over an optical image is shown in Fig. 1, illustrating the presence of six symmetrically placed vertical extensions in this galaxy. In this paper, we present new VLA D array HI data of NGC 2613 and examine them separately as well as in combination with the previously obtained C array data. The observations are presented in Sect. 2, the results, including a description of extremely large high latitude HI features and a model of the global HI distribution are given in Sect. 3, in Sect. 4, we present the discussion, including a feasibility study of a buoyancy model, and a summary is given in Sect. 5.

## 2. Observations

Details of the C array data acquisition and mapping have been given in Paper I.

The D array data were taken on Sept. 15, 2000. The flux calibrator was 3C 48 and the phase calibrator was 0837-198. The flux calibrator was also used as a bandpass calibrator and was observed once for 17 minutes at the beginning of the observing period. The phase calibrator was observed in 3 minute scans alternating with 25 minute scans on NGC 2613. The total on-source observing time was 2.4 hours and on-line Hanning velocity smoothing was applied. The data were edited, calibrated, and Fourier Transformed using natural weighting, cleaned, and continuum subtracted in the usual way using standard programs in the Astronomical Image Processing System (AIPS) of the National Radio Astronomy Observatory. The resulting (RA, DEC, Velocity) cube was then examined for broad scale structure.

The calibrated D array UV data were then combined with the previously obtained C array UV data (on-source observing time = 15.3 hours, see Paper I) to improve the signal to noise (S/N) ratio. Since the high resolution C array data have already been presented, we here concentrate on the broader scale structure by re-mapping the C+D array data, using natural weighting, over a UV range corresponding to the D array data only, i.e.  $5 \text{ k}\lambda$ . That is, we show the lower resolution results (at a typical D array resolution), but with the highest S/N possible. Table 1 lists observing and map parameters for D array and for the combined C+D array data. Note that, although we show images for the combined data set, we have inspected and analyzed all data sets both independently and in combination.

### 3. Results

Note that a full description of the C array results and relevant images have been given in Paper I and we have reproduced the zeroth moment C array map in Fig. 1. The remaining The zeroth and first moment maps from the combined data set are shown in Fig. 2, both rotated so that the x axis is parallel to the major axis of the galaxy. Vertical slices have been taken perpendicular to the major axis at positions numbered 1 through 10 in Fig. 2a and these are shown as position-velocity (PV) plots in Fig. 3. The PV slices in the last two panels of Fig. 3 show averages over the receding and advancing sides of the galaxy.

### 3.1. Tidal Tail

For the first time, we see that there is a tail of emission on the south-eastern (left, Fig. 2a) side of the galaxy which resembles tidal tails seen in galaxy interaction simulations. This tail is likely produced via an interaction with the companion, ESO 495-G017, to the north-west, whose systemic velocity is separated from that of NGC 2613 by only 143 km s<sup>-1</sup>. The tail is at negative velocities with respect to the receding side of the galaxy from which it originates and shows a strong velocity gradient along its length, becoming negative with respect to the galaxy's systemic velocity as well, i.e. the velocities become forbidden. This can occur in the case of interactions but is difficult to explain any other way. Given this velocity structure, the tail must be trailing from the eastern, receding side of NGC 2613 and is therefore in front of the galaxy. The anomalous emission seen around -200 km s<sup>-1</sup> in Slice 2, as well as the average over the receding side of the galaxy (second last panel) of Fig. 3 belongs to this tail as well. There is excess emission on the north-west (right, Fig. 2a) side of the galaxy in the vicinity of the companion, but we have found no systematic velocities associated with that emission or any other sign of a corresponding redshifted feature.

## 3.2. High Latitude HI

In Paper I, using the C array data alone, we identified and characterized the properties of 6, symmetrically placed extensions labelled F1 to F6 in Fig. 1. Fig. 2a, which includes the lower D array resolution data, now also reveal these same features on broader scales, some of which are blended with other features. Since a single cutoff level must be applied over the whole galaxy to create this image, this moment map is best used to see a global view of the disk-halo features and identify where new features might be present. The full z extents and, of course, the velocities of the individual features are best measured from PV slices perpendicular to the major axis. We have inspected many PV slices over the map and show selected slices (labelled 1 through 10 in Fig. 2a) in Fig. 3. In the new data, the previously seen features F1 through F6 occur at the same velocities and the same positions as shown in Fig. 1, after taking into account the different beam sizes and the addition of broader scale emission. Please refer to both Figs. 2a and 3 for a more thorough discussion of these features, presented below.

F1 appears similar to what has previously been seen (Fig. 1), but at lower resolution. The PV plot for F1 can be seen in Slice 2 which reveals it as a distinct feature at a velocity of 250 km s<sup>-1</sup> but it can also be seen in Slice 1 as well, extending to a projected z height of at least 100" (12.6 kpc) "above" (i.e. positive z) mid-plane. A newly seen extension immediately to the west of F1, sampled by Slice 3, may actually be associated with or part of F1, since it is seen in PV space as a small arc at about the same velocity as F1.

F2 (see Slice 1) shows several velocity components and is more complex than previously seen. Like F1, F2 extends to at least 100'' at a velocity of  $210 \text{ km s}^{-1}$ . It is not clear whether the other components may be blended with emission from the tidal tail.

F3 reveals more structure than the extension in Fig. 1 and is sampled by Slice 4 which reveals it as a 2-pronged arc above the disk centered at a velocity of 100 km s<sup>-1</sup>. Such double peaks in velocity space are typical of such features and have been seen in other galaxies (see, e.g. Lee & Irwin 1997, Lee et al. 2001).

The extension to the left of the F4 label in Fig. 2a) extends to a height 225" (28 kpc) below (i.e. negative z) mid-plane in this map. As can be seen in Slice 3 of the PV map, this feature occurs at a velocity of 50 km s<sup>-1</sup> and shows no velocity gradient with height. F4 reaches the highest z of all the extensions and, to our knowledge, reaches higher latitudes than any previously seen in an edge-on galaxy, exceeding even the starburst galaxy, NGC 5775, whose known HI features extend to  $\sim$  7 kpc from the plane (Lee et al. 2001). This is remarkable, given that NGC 2613 (log L<sub>FIR</sub> = 10.00) has a massive (0.1  $\rightarrow$  100 M<sub> $\odot$ </sub>) star formation rate that is a factor of 3 lower than that of NGC 5775 and a supernova input

energy rate per unit area that is a factor of 7 less than NGC 5775 (Irwin et al. 1999).

Feature F5 is sampled by Slices 8 and 9 and can most clearly be seen in Slice 9 as a vertical feature above the plane in PV space at a velocity of -300 km s<sup>-1</sup>. Whereas it appeared as a single extension in Fig. 1, it can now be seen to have a counterpart 55" (7 kpc) in projection farther out along the disk which is sampled by Slice 10. The counterpart clearly occurs at the same velocity and also shows no velocity gradient with height. These two features may form the base of a large loop or cylinder, similar to what has been seen in galaxies like NGC 5775 (Lee et al. 2001).

The most interesting and well-defined feature, however, is associated with F6. For example, slices 6, 7, 8 and 9 pass through a feature below the major axis which extends 22 kpc (175") in projection, from the plane and centers at -307 km s<sup>-1</sup>. Individual channel maps of this feature are shown in Fig. 4. We will refer to this as the -307 km s<sup>-1</sup> feature, rather than F6 since, as revealed by the new data, the feature is more extensive than what was originally seen in Fig. 1. This feature will be discussed extensively in Sect. 3.4.

This disk-halo emission is faint (3 - 4  $\sigma$  typically, note contour spacings in Fig. 3) but we consider the above-discussed features to be real because, 1) their spatial morphology is typical of the kinds of extensions and loops seen in other edge-on systems, 2) even though the feature might be faint far from the disk, there is evidence for disturbed contours 'beneath them' even at highly significant contour levels (see the 5th and 6th contours of Fig. 2a, for example), 3) at least the 6 major features, F1 to F6 can be seen in both independent data sets, 4) the features generally occur over several independent beams and/or velocity channels, and 5) in PV space, the features are distinct, yet smooth and connect continuously to the disk, unlike artifacts produced by a badly cleaned beam (see, e.g. the arc above the disk seen in Slice 3 of Fig. 3 at  $\sim 270 \text{ km s}^{-1}$  or the larger structures in Slices 9 and 10). In addition, 6) the Receding and Advancing panels of panels of Fig. 3) show averages over the entire advancing and receding sides of the disk, rather than just selected individual slices as shown elsewhere in the figure. In these panels, therefore, we have basically averaged together signal with noise and weak extensions would be diluted (i.e. "beam-averaged", where the beam is the size of half the galaxy). Yet these panels still show the extensions quite clearly, especially on the Advancing side where the disk-halo emission is dominated almost entirely by the -307 km s<sup>-1</sup> feature. This feature is seen up to the 4th contour which is a  $6\sigma$  detection in the diluted averaged panel. Finally, 7) for at least 4 of the 6 features, there is evidence from independent observations that extraplanar emission is present. For example, our radio continuum image (see Fig. 9 of Paper I) shows extended emission at the positions of F3, F4, F5, and F6. Also, an early HI image by Bottema (1989) at lower resolution shows extended HI emission at roughly the same locations.

The zeroth moment map of Fig. 2a also shows a number of low intensity "disconnected" features at high latitudes (for example, the emission around -300", -200"). We do not claim that all of these are real, but we have chosen to display them for the sake of comparison with future observations and because some of the emission shown in independent lower resolution images (e.g. Bottema 1989, Irwin et al. 1999) is so extended. An example would be the 'knot' of emission between F3 and F5 which is sampled by Slice 6. For this feature, the velocities are discordent with respect to the underlying disk (see Fig. 3) and therefore do not satisfy the criteria listed above.

Particularly interesting about these very high latitude features is that there is little or no evidence for any lag in velocity with z, even to very high distances from the place. The features seen below the plane in slices 3, 8, and 9 and features seen above the plane in slices 9 and 10 show no velocity gradient. The early data of Bottema (1989) also showed that the high latitude HI was co-rotating. There is some evidence, in our data, for curvature in the smaller features (cf. Slices 3 & 4 above the plane), but one could not make any case for a lag. The only slice which shows some evidence for lagging gas is Slice 1, but this slice is also closest to the tidal tail, confusing the interpretation. The averages of the advancing and receding sides of the galaxy also do not support the presence of a lagging halo. Here, we see an asymmetry in the sense of many disk-halo features on the receding side, but the advancing side is dominated by the single -307 km s<sup>-1</sup> feature. None of the features, however, show a decline with z. We investigate this further in the next section.

#### 3.3. Kinematic Models of the Global HI Distribution

We have modeled the global HI density and velocity distributions for NGC 2613 following Irwin & Seaquist (1991) and Irwin (1994). This approach models all spectra in the HI cube by adopting a volume density distribution in and perpendicular to the plane, a rotation curve and velocity dispersion (if required), and a position and orientation on the sky. Given trial input parameters describing these distributions, the routine then varies the parameters, examining the residuals, until the best fit solution is found. Various sections of the galaxy can be modeled, including galactocentric rings in the galaxy's plane. In the current version, we can also isolate slices parallel to the galaxy's plane. This permits modeling the halo, independent of the disk, which is important in this study in the event that a lagging HI halo might be present. While there is no evidence for lags in the discrete features shown in Fig. 3, it is possible that the smooth, low intensity halo might be better fit with a lagging velocity distribution, similar to what has been found for NGC 2403 (Fraternali et al. 2001). The routine, called CUBIT, interfaces to classic AIPS; potential users are requested to contact

the first author for the code.

For NGC 2613, the adopted in-plane density distribution is a gaussian ring, described by:  $n(R, z = 0) = n_0 \exp((R - R_0)^2/D^2)$ , where R is the galactocentric radius,  $R_0$  is the galactocentric distance of the center of the ring,  $n_0$  is the in-plane density at the center of the ring, and D is the scale length. D can have different values for points  $R > R_0$  $(D_o)$  and for points  $R < R_0$   $(D_i)$ . The distribution perpendicular to the plane is given by the exponential,  $n(R,z) = n(R,z=0) \exp(-z/H_e)$ , where z is the perpendicular distance from midplane and  $H_e$  is the exponential scale height. The rotation curve is described by the Brandt curve,  $V(R) = V_{sys} \pm V_{max} (R/R_{max}) (1/3 + 2/3 (R/R_{max})^m)^{(-3/2m)}$ , where  $V_{sys}$  is the galaxy's systemic velocity,  $V_{max}$  is the peak of the rotation curve occurring at a galactocentric radius of  $R_{max}$  and m is the Brandt index which is a shape parameter. A gaussian velocity dispersion,  $\sigma_V$  can also be applied, if needed. Note that a velocity dispersion will result from all contributions to line widening along the entire line-of-sight direction, for example, any non-circular motions along the plane, streaming motions due to spiral arms and local turbulence. Thus,  $\sigma_V$  may be larger than what might be expected from a local value. The above distributions result in 10 free parameters:  $n_0$ ,  $R_0$ ,  $D_o$ ,  $D_i$ ,  $H_e$ ,  $V_{sys}$ ,  $V_{max}$ ,  $R_{max}$ , m, and  $\sigma_V$ . In addition, there are 4 more orientation parameters: the position of the galaxy center, RA(0), DEC(0), the major axis position angle, PA, and the inclination, i. Over the region of the cube occupied by NGC 2613, there are 552 independent data points (beam / velocity-channel resolution elements) above a 2  $\sigma$  intensity level in the combined C+D cube, so the 14 parameters are well constrained, over all. Certain parameters may show a larger variation, however, depending on the nature of the distribution; for example,  $R_{max}$  tends to have a larger error since the point at which the rotation curve changes from rising to flat is not as well constrained by the data as some of the other parameters.

Table 2 lists the best fit modeled values for NGC 2613 for the combined C+D array data. We also modeled the C array data and D array data alone; the error bars of Table 2 reflect the variations in the parameters over the different arrays that result. Given the range of resolution over these arrays, from  $26.1'' \times 20.2''$  ( $3.3 \times 2.5$  kpc) to  $96.5'' \times 42.9''$  ( $12.1 \times 5.4$  kpc) the error bars on the modeled parameters are very small. The best fit model is shown as dashed curves superimposed on the data in Fig. 3. Taking only residuals (data cube - best fit model cube) greater than  $3\sigma$ , the root-mean-square value is 1.77 mJy beam<sup>-1</sup> and the average relative error is  $\sim 10\%$ . A zeroth moment map made from the cube of the residuals of the best fit is shown in Fig. 5.

To determine whether there are changes in i, PA, and  $H_e$  with galactocentric radius, R, we also modeled the galaxy in concentric rings. For example, either a lower value of i with increasing R (a warp) or a higher value of  $H_e$  with increasing R (i.e. a flare) could conspire

to make the halo of a galaxy appear to lag. We find that the inclination does not decrease with radius (there is a slight increase). There is indeed evidence for flaring such that, in each data set,  $H_e$  systematically increases with R. The most significant change is measured for the D array data alone such that the mean scale height between a radius of 140" and 300" (17.6 to 38 kpc) is 5.5" (693 pc) compared to a value of 1.7" (214 pc) over the whole galaxy. Thus, the disk is quite thin with a modest flare at large galactocentric radii.

In order to model the halo alone, a variety of lower and upper cutoffs to z were applied and these data were modeled in a similar fashion. (Note that z refers to the actual distance from the galaxy's midplane, not just the projected distance from the major axis.) The number of independent data points is reduced typically by about a factor of 3, depending on which z limits are chosen, but we have also held some of the parameters (the central position, position angle and systemic velocity) fixed. For the halo models, we find no evidence that  $V_{max}$  could be lower at higher z. The same conclusion is reached if the C array and D array data are modeled independently. The absence of a lagging HI halo in NGC 2613 will be discussed in Sect. 4.1.

# 3.4. The -307 km $s^{-1}$ Feature

A distinct feature occurring at -307 km s<sup>-1</sup> (see the Advancing panel of Fig. 3 and Fig. 4) has been mentioned in Sect. 3.2 and extends to a (negative) z height of 22 kpc. (This feature is also distinguishable on the major axis PV slice of Paper I). The channel maps show a complex structure below the plane, although two spurs dominate. The feature is very well defined in PV space and contributions to the feature can be seen in slices 6 through 9 which covers a range of 13 kpc in projected distance along the disk of NGC 2613 (Fig. 2a). There is also a distinct height ( $z \sim 90'' = 11$  kpc) at which the feature begins to widen abruptly in velocity (Fig. 3) and also (approximately) spatially (Fig. 4), a point we return to in the model of Sect. 4.3. Further support for HI at high z at this position comes from early HI observations by Bottema (1989) which show an HI "blob" extending to  $\sim 25$  kpc from the plane and sharing the rotation of the underlying disk. In addition, our low resolution 20 cm continuum map also shows a single large feature at this position extending 21 kpc from midplane (Irwin et al. 1999). Thus, we will treat the -307 km s<sup>-1</sup> feature to be a single, coherent structure, as implied by its appearance in PV space, centered at a projected galactocentric distance of 15.5 kpc.

This feature occurs over a restricted region of observed radial velocity ( $V_r = -307 \pm 30 \text{ km s}^{-1}$ ). Assuming that the feature originates in the disk (see Sect. 4.2), this should allow us to place limits on the position along the line of sight from which it originates since the rotation

curve of the galaxy is known. The galactocentric radius is given by  $R = R_{proj} (V(R)/V_r)$  (ignoring sin i = 0.98) where  $R_{proj}$  is the projected galactocentric radius and V(R) is the circular velocity at R which is approximately constant in this part of the galaxy (Table 2). Allowing a  $\pm 30$  km s<sup>-1</sup> range on  $V_r$ , the feature could therefore have originated from  $R = R_{proj} = 15.5$  kpc or anywhere within  $\pm 7$  kpc from this value along the line of sight, corresponding to a range of R between 15.5 and 17 kpc. Since the projected size of the feature is larger than this range (Fig. 4), it is likely that there has been some expansion with distance from the plane.

We can also put a limit on the age of the feature. Gas which leaves the disk at an earlier time should have a component of line of sight velocity corresponding to the motion of the underlying disk at that time. As the disk rotates, gas which leaves later may have a different line of sight velocity component. Consequently, there may be a gradual change in observed velocity with height (increasing or decreasing) depending on geometry. Since we see no such change, we can use the velocity half-width of the feature,  $30 \text{ km s}^{-1}$ , to place a limit on the angle over which the underlying disk has rotated over the age of the feature. We find that the feature must have formed over a timescale which is less than the time required for the disk to rotate  $\pm 24^{\circ}$  at galactocentric radii between 15.5 and 17 kpc. From the circular velocity in this region, the corresponding timescale is  $4.2 \times 10^7$  yr. These arguments will depend on how the ejected gas may or may not be coupled to the disk and should be considered order of magnitude only. Nevertheless, the result is similar to the kinematic ages found for expanding supershells in other galaxies (cf. King & Irwin 1997, Lee & Irwin 1997, Lee et al. 2001). Basically the "straightness" of the feature in PV space requires that the feature have an age << the rotation period.

The mass of this feature, as measured in PV space to the level at which the feature blends with the disk, is  $(8 \pm 2) \times 10^7 \text{ M}_{\odot}$ . Approximating the feature as a cylinder of height, 22 kpc, width and depth, 13 kpc, the mean density is  $1.1 \times 10^{-3} \text{ cm}^{-3}$ . (Reducing the diameter of the cylinder to 7.3 kpc (150") results in a mean density of  $3.6 \times 10^{-3} \text{ cm}^{-3}$ .) If the feature has reached a z height of 22 kpc in  $4.2 \times 10^7 \text{ yr}$ , the implied mean outflow velocity is 512 km s<sup>-1</sup>. The corresponding HI mass outflow rate would be 1.9 M<sub> $\odot$ </sub> yr<sup>-1</sup>.

We can also compute the potential energy of this feature (see Lee et al. 2001) which requires a knowledge of the mid-plane stellar density and scale height. Comparing the rotation curve of NGC 2613 (Chaves & Irwin 2001) to that of the Milky Way (Sofue & Rubin 2001), NGC 2613 is a factor of 4 more massive, and factor of 2 larger in radius. NGC 2613 also has a thinner disk, if we take the thickness of the HI disk (188 pc, Table 2) to be representative of the stellar thickness. Scaling the mid-plane stellar density from the Galactic value (0.185  $\rm M_{\odot}~pc^{-3}$ ) yields 0.74  $\rm M_{\odot}~pc^{-3}$  for NGC 2613 and adopting 100" (12.6

kpc) (about half the full z extent) to be representative of the height of the feature above the plane, we find a potential energy of  $1.5 \times 10^{56}$  ergs for the -307 km s<sup>-1</sup> feature. Thus, energy of this order is required to transport the cool gas to the heights observed. Although very large, this value is not unlike that determined for the largest supershells in other edge-on galaxies (cf. an input energy of  $\sim 3 \times 10^{56}$  ergs for NGC 3556, King & Irwin 1997). We return to this issue in Sect. 4.3.

#### 4. Discussion

## 4.1. The Absence of a Lagging HI Halo in NGC 2613

There are now several galaxies for which there is evidence for lagging halos. In NGC 891 ( $i \ge 88.6^{\circ}$ ), the rotation curve of the HI halo between z = 1.4 to 2.8 kpc reveals a peak velocity  $\sim 25 \text{ km s}^{-1}$  lower than in the disk (Swaters et al. 1997). In NGC 5775 ( $i = 86^{\circ}$ ), the ionized gas velocities decrease with z to heights of 5 - 6 kpc above which the velocity remains roughly constant (Rand 2000). The HI in this galaxy shows more complex structure, though lagging gas tends to dominate at z heights up to 5 to 6 kpc. Above this region, the velocities are more nearly constant or the features break up into clumps which are seen over a wide range in velocity (Lee et al. 2001). Models of NGC 2403 (inclination of 61°) suggest that a lagging halo extends to  $z \sim 3 \text{ kpc}$  (Schaap et al. 2000). Thus, from the sparse data available, the region of the lag extends to typically 3 to 6 kpc above the plane above which (if gas is detected at all) there isn't strong evidence for a global lag. Given the presence of lagging halos in these other galaxies and also some theoretical expectation of lags (cf. Bregman 1980, Benjamin 2002, Collins et al. 2002), the absence of a lagging velocity gradient along the discrete features (Sect. 3.2) and the absence of a global lag (Sect. 3.3) in NGC 2613 require comment.

Firstly, given the inclination of this galaxy (79°, Table 2) and its HI radius of  $\sim 35$  kpc, the discrete features must reach a height of z > 6.5 kpc before they will be seen beyond the projection of the disk. If it is true that lags only exist up to 3 to 6 kpc and above this there is no longer a lag (see above), then lags (if they exist) along the discrete features would be projected against the background disk. This would make a velocity gradient (if present) impossible to detect along the discrete features. The 'straightness' of the -307 km s<sup>-1</sup> feature in velocity (Fig. 3) to such high latitudes beyond the projection of the disk is, however, quite remarkable. If this feature emerges into a hot X-ray corona, as suggested in Sect. 4.3, then either the velocity of the broad-scale X-ray corona is not appreciably different from the underlying disk (although the velocity dispersion is likely much higher), or the timescale over which it could appreciably affect this gas column is greater than the age of

the feature.

As for a globally lagging halo, our kinematical model is indeed capable of detecting such a lag, even if it is projected against the disk (see Sect. 3.3) provided there is sufficient high latitude emission that halo gas can be detected at all. What we have found, however, is that NGC 2613 does not have an HI thick disk or halo. The vertical exponential scale height (188 pc, Table 2) indicates that the disk is, in fact, thin. If we create a model galaxy using the parameters of Table 2, it is straightforward to show that emission from all high latitude (z > 1 kpc) HI in fact falls below the map noise. Thus, NGC 2613 does not have a detectable lagging halo because it does not have a halo at all.

As a further comparative test, we consider the HI halo of another galaxy at the same distance, NGC 5775 ( $i = 86^{\circ}$ , D = 25 Mpc), for which we detected an HI halo with exponential scale height of 9.14" (1.1 kpc) using the same technique (Irwin 1994). If we create a model for the lower inclination ( $i = 79^{\circ}$ ) NGC 2613 in which the vertical density distribution declines exponentially from its in-disk value with the same scale height as NGC 5775, we find that it could easily have been detected, even at the lower inclination of NGC 2613.

This result illustrates the importance of using a model, rather than PV slices alone, in drawing conclusions about the possible existence of lagging halos. For example, the model can disentangle inclination effects from the effects of a thick disk. For NGC 2613, since the modeled inclination is now known to be on the low end of the range quoted in Chaves & Irwin (2000), our earlier conclusion of a lag with z can now be largely explained by projection against the background disk. This is succintly illustrated via the dashed curves in Fig. 3 which show that our thin disk model provides an almost perfect fit to the data.

## 4.2. The Discrete Features: Internal Origin and Energies

We have argued elsewhere (Paper I), largely on the basis of above/below plane symmetry (Fig. 1), that the observed features are internally generated and represent outflows. While these new data show that the galaxy is indeed interacting, it is unlikely that most of the observed features are produced via cloud impacts since the cloud would have to pass completely through the disk, forming similar structures on both sides, in contrast to what is expected theoretically (see Santillán et al. 1999). Anomalous velocities are also more likely in the case of impacts, whereas the velocities observed in NGC 2613 are typical of the underlying disk. Thus, the new data are consistent with the outflow interpretation. We cannot, however, rule out the possibility of some impacting clouds in this system and it is also possible that the interaction may assist in the process of disk-halo dynamics, for example

via stimulating a starburst or instabilities such as the Parker instability.

If the features are internally generated, their very large sizes (z up to 28 kpc, Sect. 3.2 imply exceptional energies ( $\sim 10^{56}$  ergs) which are difficult to conceive of, especially at large distances from the nuclear vicinity and in a galaxy which is not a starburst. This energy problem has been known since the first detections of Heiles Shells in the Milky Way (Heiles 1979, 1984) and has generated suggestions as far ranging as multiple supernovae and stellar winds (Heckman 2001), gamma ray bursters (Efremov et al. 1998, Loeb & Perna 1998), and jet bubbles (Gopal-Krishna & Irwin 2000) to help explain the high energies. In the following section, we suggest that the exceptional heights achieved by the features in NGC 2613 may be as much a result of the environment into which the features emerge, as to the input source itself.

# 4.3. Buoyant Outflow

The -307 km s<sup>-1</sup> feature (Fig. 3, Advancing) is remarkable in its well defined structure, in the very high latitude (22 kpc) that it achieves, and in its sudden and dramatic widening and break up in velocity at a height of  $\sim 11$  kpc. In individual slices (see slices 8 and 9, in particular), this velocity widening gives the feature a mushroom-like appearance and is reminiscent of buoyant gas rising through a higher density medium. A precedent for this kind of behaviour is the 350 pc Galactic Mushroom discovered in Canadian Galactic Plane Survey data and which has been interpreted in terms of buoyant outflow (English et al. 2000).

Given this similarity, we here consider whether buoyant outflow could explain the observed high latitude discrete HI features in NGC 2613. We present the following as a feasibility study only to see whether the results provide a reasonable match to the data using realistic parameters. We consider a match to the -307 km s<sup>-1</sup> feature only, at this time, since it is the clearest case amongst the disk halo features in NGC 2613; however, if the model is correct, it must clearly apply to the other features as well. A similar development has been presented by Avillez & Mac Low (2001) for smaller features like the Galactic Mushroom, but we here consider much larger scales (many kpc), and also include the effects of drag.

The scenario envisioned is one in which a hot, X-ray emitting corona already exists around the galaxy, possibly set up via venting through previous fountain or chimney activity. Some event or events occur within the disk which are sufficiently energetic to produce blowout. The HI is already entrained or swept up in some way by the time the outflow emerges into the halo. An initial velocity (i.e. the velocity at blow-out) could be present but is not

included here. Thus, the velocities achieved in the plume are a result only of buoyant forces. The attraction of this model is that, rather than requiring that all of the energy in the HI plume be supplied by the instigating event in the disk ( $10^{56}$  ergs, Sect. 3.4), we require only enough energy to produce the blow-out condition (e.g.  $10^{53}$  ergs, Tomisaka 1998). The remaining energy is extracted from the pressure gradient in the hot coronal gas. Ultimately, the galaxy's potential itself is providing the energy source.

Although we do not investigate the details of the entrainment or sweeping up of HI, we assume that the hot gas inside the plume carries the cool HI with it and that the density of the HI declines with z in a fashion similar to the hot buoyant plume material. In this feasibility study, we do not consider structure in the corona or outflow plume, other than the cylindrical geometry chosen for the plume, and also neglect the effects of shocks. The integrity of the HI in the presence of hot gas will be considered in the next section.

The stellar/mass density distribution of the thin disk is described by:

$$\rho_*(z) = \rho_*(0) \operatorname{sech}^2(\frac{z}{2z_*})$$

where  $z_*$  is the scale height of the stellar disk, and  $\rho_*(0)$  is the stellar density at mid-plane. Integration of Poisson's Equation:

$$\frac{dg}{dz} = -4\pi G \,\rho_*(z)$$

over the regime,  $z \gg z_*$ , together with the above density distribution, results in a gravitational acceleration which is constant with z and has a magnitude:

$$g = 8 \pi G \rho_*(0) z_* \tag{1}$$

The hot coronal gas (subscripted, c) is taken to be isothermal at temperature,  $T_c$ , with an exponential fall-off in both pressure and density, respectively:

$$P_c(z) = P_c(z_*) e^{-z/H}$$
  $\rho_c(z) = \rho_c(z_*) e^{-z/H}$  (2)

where H is the scale height. This hot coronal distribution starts at the top of the (HI + stellar) thin disk, i.e. at  $z_*$  where the outflow just blows out of the thin layer. The scale height is given by

$$H = k T_c / (g \mu m_p) \tag{3}$$

where k is Boltzmann's constant,  $\mu$  is the mean molecular weight and  $m_p$  is the mass of the proton. We consider a pure hydrogen gas ( $\mu = 1$ ) for simplicity.

Inside the plume (subscripted, i), we consider the gas to be adiabatic. The temperature gradient is:

$$\frac{dT_i}{dz} = \left(1 - \frac{1}{\gamma}\right) \frac{T_i}{P_i} \frac{dP_i}{dz} \tag{4}$$

For a plume in pressure equilibrium with its surroundings,

$$P_i(z) = P_c(z_*) e^{-z/H} (5)$$

where, again, we take the plume base to occur at  $z_*$ . Substituting Eqn. (5) and its derivative into Eqn. (4) yields:

$$T_i(z) = T_i(z_*) e^{\left(\frac{(1-\gamma)}{\gamma}\frac{z}{H}\right)}$$
(6)

and from Eqn. (5), Eqn. (6) and the perfect gas law:

$$\rho_i(z) = \rho_i(z_*) e^{-\left(\frac{z}{\gamma H}\right)} \tag{7}$$

The equation of motion (force per unit volume) of the plume material is:

$$\rho_i(z) \frac{dv}{dt} = \rho_c(z) g - \rho_i(z) g - C_D \rho_c(z) \frac{v^2}{z} - \frac{2 \eta v}{r^2}$$
 (8)

The first term on the right hand side denotes the buoyancy force, the second term gives the weight of the plume material, the third term specifies the drag force against the upper surface (assuming a case in which the effects of this force can propagate through the column) where  $C_D$  is the dimensionless drag coefficient, and the fourth term represents the viscous drag on the cylinder sides, where r is the cylinder radius and  $\eta$  is the coefficient of viscosity  $(g \, cm^{-1} \, s^{-1})$ .

Both  $C_D$  and  $\eta$  depend on the Reynolds number:

$$Re \approx 5 \times 10^{14} \frac{\rho_c(z) L v \ln \Lambda}{T_c^{5/2}}$$

assuming a pure ionized hydrogen gas, where L is a scale length above which motion is damped by viscous effects and

$$\Lambda \approx 1.3 \times 10^4 \frac{T_c^{3/2}}{n_e(z)^{1/2}}$$

where  $n_e(z)$  is the coronal electron density. Taking  $v=500 \text{ km s}^{-1}$  (Sect. 3.4) and  $T_c=2 \times 10^6 \text{ K}$ , we find for size scales, L, of order several kpc, Re is in the range  $10^{3 \to 4}$ . In this range of Re,  $C_D \sim 1$  for an incompressible fluid with cylindrical geometry. The viscosity coefficient includes both turbulent and molecular terms, i.e.  $\eta = \eta_t + \eta_m$ , where  $\eta_m = L v \rho_c(z)/Re$ 

and  $\eta_t = (Re/Re_{crit}) \eta_m$ , where  $Re_{crit}$  is the critical Reynolds number which designates the value of Re at which the flow becomes turbulent.  $Re/Re_{crit}$  is not known and depends on the geometry and nature of the interface, but typically has values between 1 and 100. We can consider whether the drag force on the cylinder sides (4th term of Eqn. (8)) is appreciable in comparison to the drag on the top of the cylinder (3rd term of Eqn. (8)). Taking  $L \sim r$ , the ratio of the 3rd to 4th drag terms becomes  $[(Re/2)(r/z)1/(1 + Re/Re_{crit})]$ . Since r is of order z, then for  $Re \sim 10^{3 \to 4}$ , even  $Re/Re_{crit}$  up to 100 ensures that the drag at the top will dominate over that at the sides. Therefore the 4th term in Eqn. (8) is small and will be neglected.

Substituting v = dz/dt,  $\mathcal{R}(z_*) = \rho_c(z_*)/\rho_i(z_*)$ , and  $\gamma = 5/3$  into Eqn. (8) and rearranging yields:

$$\frac{dv}{dz} = \mathcal{R}(z_*) e^{-0.4\frac{z}{H}} \frac{g}{v} - \frac{g}{v} - \mathcal{R}(z_*) e^{-0.4\frac{z}{H}} \frac{v}{z}$$
(9)

This equation was integrated numerically for the input parameters shown in Table 3, yielding the curves of v(z) and z(t) shown in Fig. 6 and Fig. 7, respectively. The stellar scale height,  $z_*$  is set to 188 pc (Table 2) and we consider a coronal temperature,  $T_c = 2.5 \times 10^6$  K (Models 1 to 4) which is comparable to that found from X-ray observations of NGC 253 (Pietsch et al. 2000) as well as a temperature which is a factor of 2 higher (Model 5). Since the midplane stellar density of  $0.74 \,\mathrm{M_\odot}$  pc<sup>-3</sup> is a value which has been scaled from Galactic values, given the size and mass of NGC 2613 (see Sect. 3.4), we also consider a slightly lower value (Models 3 and 4). The behaviour of the curves depends only on the density ratio at the base of the corona,  $\mathcal{R}(z_*)$ , rather than the individual densities, but we can additionally fix the density at the bottom of the corona,  $n_c(z_*)$  to be equal to the HI density at the top of the thin disk at the position of the plume (see Table 2), providing constraints upon the density within and outside of the plume. The peaks of the velocity curves (Fig. 6) indicate where the acceleration of the plume material goes to zero; we define the z height at which this occurs to be  $z_{stall}$ . This position should correspond to the point at which the plume widens in velocity space, observationally determined to be  $\sim 11 \,\mathrm{kpc}$ .

Models 1 and 2 (Fig. 6) show the effect of changing the initial density ratio, such that the lower ratio (Model 2) results in a lower maximum velocity and a lower  $z_{stall}$  (7.4 kpc as compared to 11.9 kpc). A comparison of Models 1 and 3 or of Models 2 and 4 show the effect of decreasing the midplane mass density. This lowers the gravitational acceleration (Eqn. (1)) which lowers both the buoyancy and the weight of the plume material. It also increases the scale height (Eqn. (3)) which increases both the buoyancy and the drag. The net effect is higher  $z_{stall}$  at lower g for the range of parameters given here. A comparison of Models 1

and 5 shows the effect of increasing the coronal gas temperature. The higher temperature increases the scale height alone (Eqn. (3)) which, again, increases both buoyancy and drag. Since drag is velocity dependent, the net effect is that the peak velocities achieved are lower for higher coronal temperatures.

Clearly, Models 1, 4, and 5 provide an adequate match to the observed  $z_{stall}$ . Model 1, however, results in a mean plume density (between  $z_*$  and  $z_{stall}$ ) of only  $0.27 \times 10^{-3}$  cm<sup>-3</sup> whereas the HI density alone is  $\sim 1 \times 10^{-3}$  (Sect. 3.4), and is therefore not realistic. Models 4 and 5 both result in reasonable fits to the known observational parameters, with Model 5 slightly preferred because of its higher internal plume density (higher than that of the HI alone) and lower internal temperature. Note that the mean internal temperature derived here ( $\sim 10^7$  K) is comparable to the hot (T = 1.2 keV = 1.4 × 10<sup>7</sup> K) component of the outflow in NGC 253 (Pietsch et al. 2000). The peak velocities derived here ( $\sim 250$  to 300 km s<sup>-1</sup>) are lower than the gross estimate of 500 km s<sup>-1</sup> computed in Sect. 3.4 since we only model the feature up to the stall height (11 kpc) rather than over its total length. The timescales of  $\sim 5$  to 6 × 10<sup>7</sup> yr (Fig. 7) are in good agreement with the estimate found from the kinematical structure of the plume (4 × 10<sup>7</sup> yrs). The mass outflow rate to the stall point is  $\sim 1 \text{ M}_{\odot} \text{ yr}^{-1}$ . Mass flow continuity requires that the plume of Model 5 should increase in radius by a factor of 1.8 between z heights of 4.7 and 11.1 kpc.

## 4.4. Integrity of the HI

It is unlikely that the HI will be uniformly distributed at its mean density of  $\sim 10^{-3}$  cm<sup>-3</sup> but may exist in denser clouds or clumps whose sizes and distribution are not described by this simple model. In general, however, the situation will be not unlike that of those high velocity clouds (HVCs) which are in the hot halo of the Milky Way and the same issues regarding whether or not the clouds can remain neutral must be considered. Photoionization of the HI by starlight should be negligible, considering the high galactic latitudes achieved. As pointed out by Murali (2000), the relevant interactions are HI - proton and HI - electron interactions for which the interaction cross-sections are in the range  $\sigma = 10^{-16}$  to  $10^{-15}$  cm<sup>-2</sup> for a relative velocity of order 200 km s<sup>-1</sup> as is appropriate here. The mean free path into the HI cloud is then  $l = 1/(n_c \sigma) = 0.3$  to 3 pc or smaller if the HI is clumped. This is considerably smaller than the size scale of the plume and therefore these ionizing interactions should be minor.

The most important interaction will be heating due to thermal conductivity leading to the evaporation of clouds. The classical mass evaporation rate, applicable to the case in which the mean free path is small in comparison to cloud size, is given, for approximately spherical clouds, by  $\dot{m}=2.75\times 10^4~{\rm T}^{5/2}~{\rm R}_{pc}~\phi~{\rm g~s}^{-1}$ , where T is the temperature of the external medium,  ${\rm R}_{pc}$  is 1/2 of the largest dimension of the cloud in parsecs, and  $\phi$  is a parameter which measures the inhibition of heat flux due to the magnetic field and cloud geometry (Cowie & McKee 1979, Cowie et al. 1981). We will assume  $\phi=1$  (no inhibition) which maximizes the evaporation rate. Using  $T=2.5\times 10^6~{\rm K}$  and  $R=5\times 10^3~{\rm pc}$  we find  $\dot{m}=0.021~{\rm M}_{\odot}~{\rm yr}^{-1}$  (to within factors of a few, given the different geometry). The timescale for complete evaporation of the  $8\times 10^7~{\rm M}_{\odot}$  HI plume at a constant rate is then M/  $\dot{m}=4\times 10^9~{\rm yr}$ . Since this is two orders of magnitude larger than the age of the plume, we expect that the plume will not evaporate over its lifetime. A caveat, however, is that since M/  $\dot{m}$   $\propto {\rm R}^2$ , if HI is distributed in many smaller clouds, then the evaporation time could approach the age of the plume.

## 4.5. The X-ray Corona

If the HI is indeed reaching such high values of z because of buoyancy, then HI diskhalo features probe the parameters of the halo gas, as suggested in Sect. 1. We have so far considered only whether buoyancy is feasible. There may be other dynamics at work as well (for example, an initial velocity at blow-out or magnetic fields) and the proposed hot corona is also unlikely to have the smooth distributions postulated here. Nevertheless, in the context of the model, it is interesting to predict the X-ray luminosity of the corona in the vicinity of the plume.

For the case in which the ion and electron densities are equal, the index of refraction is 1, the charge Z=1, the frequency is greater than the plasma frequency, and  $T>3.6\times10^5$  K, then:

$$L_x = 3.7 \times 10^{-38} V \frac{n_e^2}{T^{1/2}} \int ln[4.7 \times 10^{10} (T/\nu)] exp(-h\nu/kT) d\nu$$
 ergs s<sup>-1</sup>

(Lang 1999), where V is the source volume and  $n_e$  is the electron density. Taking the limits of integration to be over the soft X-ray band (0.2 to 2.5 keV) and  $T_c = 5 \times 10^6$  K, (Model 5), the above becomes:

$$L_x = 2 \times 10^{36} \left(\frac{V}{\text{kpc}^3}\right) \left(\frac{n_e}{0.01 \text{ cm}^{-3}}\right)^2 \text{ ergs s}^{-1}$$

A mean coronal density (between  $z_*$  and  $z_{stall}$ ) of 0.035 cm<sup>-3</sup> (Model 5, Table 3) in a rectangular region roughly the size of the modeled region of the plume (11 kpc × 13<sup>2</sup> kpc) provides an estimate of the soft X-ray luminosity of  $L_x = 4.6 \times 10^{40}$  erg s<sup>-1</sup>. Using instead the density at  $z_{stall}$  of  $2.8 \times 10^{-3}$  cm<sup>-3</sup> gives  $L_x = 2.9 \times 10^{38}$  erg s<sup>-1</sup>. The X-ray luminosities

of the hot gas in NGC 253 and M 82 are  $2 \times 10^{39}$  erg s<sup>-1</sup> and  $2 \times 10^{40}$  erg s<sup>-1</sup>, respectively (Pietsch et al. 2000). Thus, the predicted X-ray halo for NGC 2613 should be observable below height,  $z_{stall}$ , though is unlikely to have the smooth exponential distribution envisioned in this simple model. Note that NGC 2613 is more than an order of magnitude more massive than M 82 and therefore is more likely to retain any hot gas which might be around it. The values computed here will be lower, of course, if some other effect is contributing to the outflow.

#### 4.6. Blowout of Disk Gas

The results of Table 3 show that it is feasible to transfer large masses to high galactic latitudes via buoyancy in a postulated X-ray corona. This drastically reduces the computed input energy requirements since it is no longer necessary to eject large masses to high altitudes. It is only necessary to achieve blow-out through the thin HI disk of NGC 2613. The conditions required for blow-out have been investigated by a variety of authors (see Tomisaka 1998, for example) but energy requirements are typically of order  $10^{53}$  ergs, rather than the  $10^{56}$  ergs that would normally be required for the -307 km s<sup>-1</sup> feature.

While the details of the interaction between the HI and hot outflowing gas are beyond the scope of this paper, it is important to ask whether there would originally have been sufficient HI in the disk from which the  $8 \times 10^7 \,\mathrm{M_\odot}$  in the -307 km s<sup>-1</sup> feature could have been swept up. Assuming cylinderical geometry, a disk region of radius, 6.5 kpc (Sect. 3.4) and using the modeled density and thickness of the disk (Table 2), the available HI mass is  $\sim 3 \times 10^8 \,\mathrm{M_\odot}$  suggesting that  $\sim 26\%$  of the disk mass is swept up. This fraction would be higher for cone-like outflow.

We should also consider whether the mass outflow rate is consistent with that of a galactic fountain. The estimated HI mass outflow rate (Sect. 3.4, Sect. 4.3) is  $\sim 1$  to 2  $\rm M_{\odot}$  yr<sup>-1</sup>. Thus, the combined HI + hot gas outflow rate will be of order several  $\rm M_{\odot}$  yr<sup>-1</sup>. Collins et al. (2002) have estimated the mass flow rate for the diffuse ionized gas (DIG) component in a galactic fountain, assuming a ballistic model of gas clouds. They find global values of  $\dot{M} = 22 \sqrt{f_V/0.2} \rm \ M_{\odot} \rm \ yr^{-1}$  for NGC 891 and  $\dot{M} = 13 \sqrt{f_V/0.2} \rm \ M_{\odot} \rm \ yr^{-1}$  for NGC 5775, where  $f_V$  is the filling factor. If these global values apply to a 20 kpc radius disk, taking  $f_V = 0.2$  and scaling to the disk area of the -370 km s<sup>-1</sup> feature yields mass outflow rates of 1.4 and 2.3  $\rm \ M_{\odot} \rm \ yr^{-1}$  which are comparable to what we estimate, above. It is not yet clear, however, whether these galactic fountain values can be directly scaled to the relevant regions of NGC 2613. It may be that some additional source of pressure is still required, for example, magnetic fields in the form of a Parker instability. If such fields continue to rise

into the corona, the inclusion of this magnetic pressure would relax (i.e. lower) the density or temperature requirements internal to the plume (Table 3).

### 5. Conclusions

New VLA D array data of NGC 2613 have been combined with previous higher resolution observations (Chaves & Irwin 2001) to show a more extensive HI distribution than previously observed. The galaxy is now seen to have a tidal tail on its eastern side due to an interaction with its companion, ESO 495-G017, to the north-west.

The three-dimensional HI distribution in NGC 2613 has been modeled following Irwin & Seaquist (1991) and Irwin (1994), a method which allows the volume density distribution to be determined as well as the scale height and inclination to be disentangled. We find that the inclination of the galaxy (79°) is on the low end of the range given in Chaves & Irwin (2001) and the model now shows that there is no HI halo in NGC 2613. Rather, the global HI distribution is well fit by a thin disk of exponential scale height,  $z_e = 188$  pc. The use of such a model is very important in drawing conclusions about the presence or absence of a global halo in a galaxy of this inclination. Previous reports of a lagging halo from PV slices alone can largely be attributed to projection against the background disk.

While there is no significant global HI halo in NGC 2613, there are more discrete disk-halo HI features than previously detected and these HI features achieve extremely high latitudes. Even though a tidal interaction is occurring, we suggest that most of the discrete kpc-scale features have been produced internally rather than from impacting clouds, although we do not rule out the possiblity of the companion galaxy having some indirect effect (e.g. triggering instabilities). The presence of many discrete features may be related to the fact that the global HI disk is thin, favouring blow-out. The observed z heights are quite remarkable (e.g. up to 28 kpc). The -307 km s<sup>-1</sup> feature, in particular, below the plane on the advancing side, reaching 22 kpc in z height and of total mass,  $(8 \pm 2) \times 10^7 \,\mathrm{M}_{\odot}$ , is very obvious and well-defined in PV space. Its center is likely close to its projected radius of 15.5 kpc and it extends over a large ( $\pm$  7 kpc radius) projected galactocentric radius. If this feature has achieved its z height as a result of internal processes, then extremely large energies are required,  $\sim 10^{56} \,\mathrm{ergs}$ .

Given the very high input energies required for the -307 km s<sup>-1</sup> feature, its resemblance to smaller buoyant features (cf. the Galactic Mushroom, English et al. 2000), and the fact that X-ray halos are being found around an increasing number of star forming spiral galaxies, we have carried out a feasibility study as to whether this feature can be interpreted

as an adiabatic buoyant plume. The observed HI would be carried out by a hot, low density outflowing gas and, after having achieved blowout, would rise through a hot pre-existing X-ray corona. A reasonable example (Model 5), has a mean plume temperature and density of  $1 \times 10^7$  K and  $5.5 \times 10^{-3}$  cm<sup>-3</sup> rising into a hot isothermal corona of temperature and mean density,  $5 \times 10^6$  K and 0.035 cm<sup>-3</sup>, respectively. These conditions produce a stall height of 11 kpc which is where the observed plume widens in velocity and position space. The coronal density at the stall height is  $2.8 \times 10^{-3}$  cm<sup>-3</sup>. The maximum outflow velocity in this model is 290 km s<sup>-1</sup> and it reaches the stall height in  $5.4 \times 10^7$  yrs. This model shows that, even with buoyancy alone (and there may be additional sources of pressure such as magnetic fields), HI can reach these extreme z heights.

The advantage of such a model is that the energy requirements from the initial event are drastically reduced to being only what is required for blowout, a reduction of several orders of magnitude. The energy is largely extracted from the gravitational potential of the galaxy rather than the initial event within the disk. The behaviour of the plume should sample the parameters of the X-ray corona. The predicted X-ray luminosity suggests that the corona should be observable at heights below the stall height although we expect that the distribution of X-ray emission may not be as smooth as assumed by the model.

JI wishes to thank the Natural Sciences and Engineering Research Council of Canada for a research grant. We are grateful to Dr. R. N. Henriksen for fruitful and envigorating discussions. Thanks also to Mustapha Ishak for assistance with MAPLE.

#### REFERENCES

Benjamin, R. 2002, in "Seeing through the Dust", ASP Conf Series, ed. A. R. Taylor, T. L. Landecker, & T. Willis

Bottema R. 1989, A&A, 225, 358

Bregman J. N. 1980, ApJ, 236, 577

Chaves T. A., & Irwin J. A. 2001, ApJ, 557, 646 (Paper I)

Collins J. A., Rand R. J., Duric N., & Walterbos R. A. M. 2000, ApJ, 536, 645

Collins J. A., Benjamin R. A., & Rand R. J. 2002, in press

Cowie L. L., & McKee C. F. 1977, ApJ, 211, 135

Cowie L. L., McKee C. F., & Ostriker J. P. 1981, ApJ, 247, 908

de Avillez M. A., & Berry D. L. 2001, MNRAS, 328, 708

Duric N., Irwin J., & Bloemen H. 1998, A&A, 331, 428

Efremov Y. N., Elmegreen B. G., & Hodge P. W. 1998, ApJ, 501, L163

English J., Taylor A. R., Mashchenko S. Y., Irwin J. A., Basu S., & Johnstone D. 2000, ApJ, 533, L25

Fraternali F., Oosterloo T., Sancisi R., & van Moorsel G. 2001, astro-ph 0110369

Gopal-Krishna, & Irwin J. A. 2000, A&A, 361, 888

Heckman T. 2001, in Gas and Galaxy Evolution, ASP Conf. Series, Vol. 240, (San Francisco: ASP), ed. J. E. Hibbard, M. P. Rupen, & J. H. van Gorkom, 345

Heiles C. 1979, ApJ, 229, 533

Heiles C. 1984, ApJS, 55,585

Irwin J. A. 1994, ApJ, 429, 618

Irwin J. A., English J., & Sorathia B. 1999, AJ, 117, 2102

Irwin J. A. & Seaquist E. R. 1991, ApJ, 371, 111, Erratum ApJ, 415,415

King D. L., & Irwin J. A. 1997, NewA, 2, 251

Lang K. 1999, Astrophysical Formulae (Springer: Berlin)

Lee S.-W, & Irwin J. A. 1997, ApJ, 490, 247

Lee S.-W., Irwin J. A., Dettmar R.-J., Cunningham C. T., Golla G., & Wang Q. D. 2001, A&A, 377, 759

Loeb A., & Perna R. 1998, ApJ, 503, L135

Lotz W. 1967, ApJS, 14, 207

Murali C. 2000, ApJ, 529, L81

Olling R., & Merrifield M. R. 2000, MNRAS, 311, 361

Pietsch W., Vogler A., Klein U., & Zinnecker H. 2000, A&A, 360, 24

Rand R. J. 2000, ApJ, 494, L45

Santillán A., Franco J., Martos M., & Kim J. 1999, ApJ, 515, 657

Schaap W. E., Sancisi R., & Swaters R. A. 2000, A&A, 356, L49

Sofue Y. & Rubin V. 2001, ARA&A, 39, 137

Swaters R. A., Sancisi R., & van der Hulst J. M. 1997, ApJ, 491, 140

Tomisaka K. 1998, MNRAS, 298, 797

Tüllmann R., Dettmar R.-J., Soida M., Urbanik M., & Rossa J. 2000, A&A, 364, L36

This preprint was prepared with the AAS LATEX macros v5.0.

Fig. 1.— VLA C array HI Column density map of NGC 2613 superimposed on a Digitized Sky Survey optical image, from Paper I. Extensions are marked F1 through F6.

Fig. 2.— (a) HI total intensity (zeroth moment) map of NGC 2613 from the combined C+D array data, rotated so that the major axis is horizontal. The central positions of NGC 2613 and its companion, ESO 495-G017, are marked with crosses. The map was formed by first smoothing the data by 3 channels in velocity and 11 pixels ( $\sim 1.4$  beams, 1 pixel = 5") spatially, applying a cut off of 0.35 mJy beam<sup>-1</sup> to the smoothed, lower rms cube, and then summing the unsmoothed data excluding those points that fell below the cutoff. The greyscale ranges from 0 to 3000 Jy beam<sup>-1</sup> m s<sup>-1</sup> and contours are at 20, 30, 50, 90, 150, 250, 500, 1200, 2150, 2800 and 3200 Jy beam<sup>-1</sup> m s<sup>-1</sup> (1 Jy beam<sup>-1</sup> m s<sup>-1</sup> = 7.375  $\times$  10<sup>17</sup> cm<sup>-2</sup>). Vertical numbered lines indicate where the slices were taken for the PV plots of Fig. 3 and the features, F1 to F6 are again labelled. (b) The intensity-weighted mean velocity field (first moment map). Contours, in units of km s<sup>-1</sup> are marked. This map was made in the same fashion as (a) but the cutoff was set to 0.45 mJy beam<sup>-1</sup>.

Fig. 3.— Position-velocity plots corresponding to the numbered vertical slices shown in Fig. 2. Solid curves represent the data and red dashed curves represent the best fit model (see Table 2). The velocity is with respect to the systemic velocity. Contours are at  $0.65~(1.5\sigma)$ , 0.85, 1.1, 1.5, 3, 6, 10, 15, and  $22~\text{mJy beam}^{-1}$ . Negative contours (not shown) are randomly distributed over the images. The last two panels show an average over 250'' for the receding and advancing sides, respectively. For these, contours are at  $0.2, 0.35, 0.6, 0.9, 2, 3, 4.5, 6, 10, \text{ and } 15~\text{mJy beam}^{-1}$  and the rms noise is  $\sim 0.16~\text{mJy beam}^{-1}$ .

Fig. 4.— Sequence of 4 channels on the advancing side of the galaxy showing the -307 km/s feature with contours and greyscale chosen to highlight this feature. Contours are at -0.9, 0.9 (2 $\sigma$ ), 1.2, 1.5, 1.9, 3, 6, and 10 mJy beam<sup>-1</sup> and the greyscale ranges from 0.45 (1 $\sigma$ ) to 10 mJy beam<sup>-1</sup>. Velocities are marked at the top right of each panel.

Fig. 5.— Zeroth moment map of the residuals (data cube - best fit model cube) l for all points  $> 3\sigma$ . Solid curves represent excess data and dashed curves represent excess model, with contours at -800, -600, -400, -200, -100, 100, 200, and 400 Jy beam<sup>-1</sup> m s<sup>-1</sup>.

Fig. 6.— Velocity as a function of z height for the five buoyancy models, Model 1 (crosses), Model 2 (diamonds), Model 3 (circles), Model 4 (boxes) and Model 5 (points), whose parameters are given in Table 3.

Fig. 7.— z height as a function of time for the five buoyancy models, Model 1 (crosses), Model 2 (diamonds), Model 3 (circles), Model 4 (boxes) and Model 5 (points), whose parameters are given in Table 3. The integration of these curves have been halted at  $z_{stall}$ .

Table 1. Observing and Map Parameters.

Parameter	D Array	C+D Array	
No. velocity channels	63	63	
Velocity Resolution (km s <sup>-1</sup> )	20.84	20.84	
Total Bandwidth (MHz)	6.25	6.25	
Synthesized Beam			
major $\times$ minor axis (" $\times$ ") @ PA ( $^{\circ}$ )	$96.5\times42.9$ @ -21.6	$47.1\times32.1$ @ -8.2	
Rms noise/channel (mJy beam <sup>-1</sup> )	0.93	0.45	
Rms noise/channel (K)	0.14	0.18	

Table 2: Modeled Kinematic and Density Parameters for Combined C+D Array Data.

Parameter	Whole Galaxy <sup>a</sup>	
RA (J2000) (h m s)	$08\ 33\ 22.8\pm0.3$	
DEC (J2000) (° ' ")	$-22\ 58\ 29\ ^{+4}_{-2}$	
PA (°)	$114.2^{\ +0.8}_{\ -0.1}$	
i (°)	$79.2^{+0.7}_{-0.1}$	
$V_{sys} (km s^{-1})$	$1663^{+8}_{-1}$	
$V_{max} (km s^{-1})$	$304 \pm 4$	
$R_{max}$ (")	$112^{\ +1}_{\ -59}$	
m	$0.51  {}^{+0.05}_{-0.35}$	
$\sigma_V \; ({\rm km \; s^{-1}})$	$17 \pm 5$	
$n_0 (cm^{-3})^b$	$0.43^{+0.01}_{-0.26}$	
$R_0$ (")	$140 \pm 5$	
$D_o$ (")	$95^{\ +1}_{\ -5}$	
$D_i$ (")	$81  {}^{+15}_{-3}$	
$H_e$ (")	$1.5  {}^{+2.0}_{-0.1}$	

 $<sup>^</sup>a$ Errors reflect the variation in the parameter that results when the C array and D array data are modeled separately, and so throughout.

 $<sup>^</sup>b\mathrm{The}$  density is the mean over the physical region corresponding to a 5" by 5" by 20.84 km s $^{-1}$  (RA, DEC, Velocity) voxel.

Table 3: Buoyancy Model Parameters.

Parameter	Model 1	Model 2	Model 3	Model 4	Model 5
$T_c (10^6 \text{ K})$	2.5	2.5	2.5	2.5	5.0
$\rho_*(0) \ (M_{\odot}  pc^{-3})$	0.74	0.74	0.50	0.50	0.74
$H^a(kpc)$	1.4	1.4	2.1	2.1	2.8
$\mathcal{R}(z_*)$	100	20	100	20	10
$n_c(z_*)^b \text{ (cm}^{-3})$	0.15	0.15	0.15	0.15	0.15
$n_i(z_*) \text{ (cm}^{-3})$	0.0015	0.0075	0.0015	0.0075	0.015
$z_{stall} \text{ (kpc)}$	11.9	7.4	17.5	11.0	11.1
$\overline{n_c}^c  (\mathrm{cm}^{-3})$	0.015	0.025	0.016	0.026	0.035
$n_c(z_{stall})^d (10^{-3} \text{ cm}^{-3})$	0.031	0.76	0.036	0.80	2.8
$\overline{n_i}^e (10^{-3} \text{ cm}^{-3})$	0.27	2.1	0.28	2.2	5.5
$\overline{T_i}^f (10^7 \text{ K})$	6.8	2.0	6.9	2.0	1.2

Note. — See Sect. 4.3 for an explanation of the parameters. a) computed from Eqn. (3) and Eqn. (1) using  $z_* = 188$  pc (Table 2). b) The coronal density at  $z_*$  (the top of the thin disk) is computed from the parameters of the HI distribution at the position of the plume (see Table 2). c) The mean coronal density is determined from Eqn. (2), over the region from  $z_*$  to  $z_{stall}$ . d) The coronal density at height,  $z_{stall}$  from Eqn. (2). e) The mean plume density is determined from Eqn. (7), over the region from  $z_*$  to  $z_{stall}$ . f) The mean plume temperature is determined from Eqn. (6), over the region from  $z_*$  to  $z_{stall}$ .

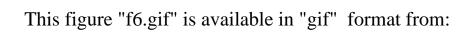
This figure "f1.gif" is available in "gif" format from:

This figure "f2.gif" is available in "gif" format from:

This figure "f3.gif" is available in "gif" format from:

This figure "f4.gif" is available in "gif" format from:

This figure "f5.gif" is available in "gif" format from:



This figure "f7.gif" is available in "gif" format from: